Title

Beyond structure: Deciphering site-specific dynamics in proteins from double histidine-based EPR measurements.

Journal

Protein Science, 31(7)

Authors

Singewald, Kevin

Wilkinson, James

Hasanbasri, Zikri

et al.

Publication Date

2022-07-01

DOI

10.1002/pro.4359

Peer reviewed

Received: 28 March 2022 | Revised: 16 May 2022 | Accepted: 20 May 2022

DOI: 10.1002/pro.4359

METHODS AND APPLICATIONS

Beyond structure: Deciphering site-specific dynamics in proteins from double histidine-based EPR measurements

Kevin Singewald | **James A. Wilkinson** | **Zikri Hasanbasri** | **Sunil Saxena**

Department of Chemistry, University of Pittsburgh, Pittsburgh, PA, USA

Correspondence
Sunil Saxena, Department of Chemistry, University of Pittsburgh, Pittsburgh, USA
Email: sksaxena@pitt.edu

Funding information
Division of Molecular and Cellular Biosciences, Grant/Award Number: NSF BSF MCB: 2006154

Review Editor: Carol Post

Abstract

Site-specific dynamics in proteins are at the heart of protein function. While electron paramagnetic resonance (EPR) has potential to measure dynamics in large protein complexes, the reliance on flexible nitroxide labels is limitating especially for the accurate measurement of site-specific β-sheet dynamics. Here, we employed EPR spectroscopy to measure site-specific dynamics across the surface of a protein, GB1. Through the use of the double Histidine (dHis) motif, which enables labeling with a Cu(II) – nitrilotriacetic acid (NTA) complex, dynamics information was obtained for both α-helical and β-sheet sites. Spectral simulations of the resulting CW-EPR report unique site-specific fluctuations across the surface of GB1. Additionally, we performed molecular dynamics (MD) simulations to complement the EPR data. The dynamics observed from MD agree with the EPR results. Furthermore, we observe small changes in $g_{||}$ values for different sites, which may be due to small differences in coordination geometry and/or local electrostatics of the site. Taken together, this work expands the utility of Cu(II)NTA-based EPR measurements to probe information beyond distance constraints.

1 | INTRODUCTION

The innate ability of a protein to protect the cell, catalyze reactions, transport chemicals or other biomolecules, or perform other intrinsic functions depends critically on its structure as well as site-specific dynamics.[1–3] The central dogma states that function is derived from protein structure, whether to form a specific binding site or to undergo a conformational change. However, these proteins do not exist in only one state but instead exist in multitude of microstates or even macrostates that describes the "on" and "off" states of the proteins.[4] For example, myoglobin goes through various microstates at a 0.1-ns timescale to allow oxygen bind and unbind as the protein delivers oxygen throughout the body.[5] Another example is adenylate kinase where the reversible conversion of AMP and ATP into two ADP molecules depends on backbone motions in the scale of 0.75 to 1.68 ns.[6] The population of "on" and "off" states and the transitions between these states are described by the dynamics of the protein. The interplay between dynamics and function is further emphasized in many other studies that examine protein oligomerization, functional dynamics in enzymes, and ligand recognition.[7–14] Most often, this insight is obtained through NMR.[15] Despite the successes of NMR, measurement of dynamics can be difficult for large proteins and proteins exhibiting widespread microsecond–millisecond dynamics that broaden peaks.[16–19] On the other hand, electron paramagnetic resonance (EPR) has increasingly become important for the measurement of site-specific protein dynamics. EPR is sensitive to site-specific protein dynamics at a ns to μs timescale.[20,21] Furthermore, EPR can be used even on large biomolecules that are sometimes inaccessible to NMR.

As a tool to measure site-specific protein dynamics, EPR emerged largely due to site-directed spin labeling.[22]

Here, residues are selectively labeled with an EPR-active spin probe to provide residue-specific information. These measurements most often utilize cysteine residues labeled with the MTSL nitroxide radical, resulting in the R1 side chain.[23–25] The R1 side chain has high intrinsic flexibility due to the side chain containing five rotatable bonds between the protein backbone and the unpaired electron. In the specific case of solvent-exposed α-helical sites, the measurement of site-specific dynamics are based on the ansatz that the R1 side chain fluctuations undergo similar internal motions.[25–27] Therefore, any changes in EPR lineshapes for solvent-exposed α-helical sites can be attributed to changes in backbone dynamics. However, this attribution is invalid for sites on β sheets since the internal motions and rotameric preferences of R1 are influenced by nearby side chains.[28–31] More rigid bifunctional spin labels work to overcome this limitation but require complex labeling schemes.[32–34] Additionally, both R1 and bifunctional labels are reliant on selective cysteine labeling which may require other native cysteines to be mutated away. Such a need for a "cys-null" protein can be problematic if native cysteine residues are abundant or are required for function.[35,36] Therefore, EPR-based dynamics measurements benefit from an alternative label that requires noncysteine functionalization, reports directly on β-sheet sites, and is simple to implement.

A strong candidate to overcome these complications is Cu(II)-dHis labeling. This labeling scheme relies on the generation of protein mutants with two strategically placed histidine residues positioned on residues i and i + 2 for β sheets, and i and i + 4 for α helices, known as the dHis motif.[37] The dHis mutation results in a rigid attachment of the Cu(II) probe to the protein with no complex synthesis scheme.[37,38] Thus, the Cu(II) labeling method is applicable to proteins where cysteine mutagenesis may be problematic. Additionally, the Cu(II) atom is complexed with nitrilotriacetic acid (NTA) to selectively chelate to the dHis motif.[39] Furthermore, the labeling can be implemented in a number of buffers,[40] at a range of pH between 6.4 and at least 8.4, and is relatively resistant to the presence of competitor ions.[41]

The rigid dHis-Cu(II)NTA label is an incisive tool in distance measurements from pulsed EPR, providing narrow distance distributions that dramatically improve the resolution of EPR methodology.[37,42] The measured distance between Cu(II) spin probes has uncovered the location of native metal binding sites using fewer distance constraints than R1, observed subtle conformational changes unresolved by similar R1-based measurements, and determined the relative orientations between two sites in a protein.[8,43–45] Additionally, distance measurements on a Cu(II)NTA-labeled protein can be acquired at submicromolar concentrations.[46,47]

More recent work has also introduced the potential of dHis-based labeling to measure site-specific dynamics in proteins.[48] While these data show promise, the development of this methodology requires several additional considerations. First, only three sites on a protein were explored previously. Therefore, a more extensive examination is necessary to properly decipher trends across a helix or a sheet, and to compare the EPR data with prior knowledge. Second, a more extensive labeling across several sites of a protein allows for a more comprehensive development of the characteristic magnetic parameters (*g* and hyperfine tensors) for this spin label, which can provide new insight. Finally, previous experiments were obtained in a suboptimal buffer, Tris buffer,[40] which can potentially complicate labeling. In this work, we account for all these considerations. We generated nine unique, solvent-exposed dHis mutations and labeled with Cu(II) NTA. We acquired *g* and hyperfine values from CW-EPR at 80 K and simulated correlation times from room temperature CW-EPR. Finally, we provide complimentary MD simulations to support observations from the CW-EPR. Taken together, we demonstrate the utility of the dHis motif as a biophysical tool in measuring site-specific dynamics.

2 | RESULTS AND DISCUSSION

2.1 | 80 K CW-EPR spectra

All EPR experiments were performed on the immunoglobulin-binding domain of protein G (GB1). GB1 is a well-behaved and thoroughly understood globular protein with mostly rigid residues.[49–51] Subsequently, GB1 has been used extensively to develop site-directed Cu(II) labeling using the dHis motif.[37,48,52,53] In addition, information on the structure and dynamics of R1-labeled GB1 is also available.[28,29,54] As shown in Figure 1, GB1 contains 56 amino acids over four β sheets and one α helix.[55] Additionally, there is a hydrophobic core spanning the C-terminal end of β1, N-terminal end of β3, β4, and the buried sites of the α helix. These hydrophobic cores are often vital in protein stability, as simply mutating a single hydrophobic residue into another hydrophobic residue can alter internal protein affinity by four orders of magnitude.[56] Around the hydrophobic core are a series of charged and polar residues on β2, both ends of β3, and the solvent-exposed sites of the α helix. In Figure 1a, the positively charged residues are indicated by red, and the negatively charged residues are blue, while the nonpolar residues are colored yellow.

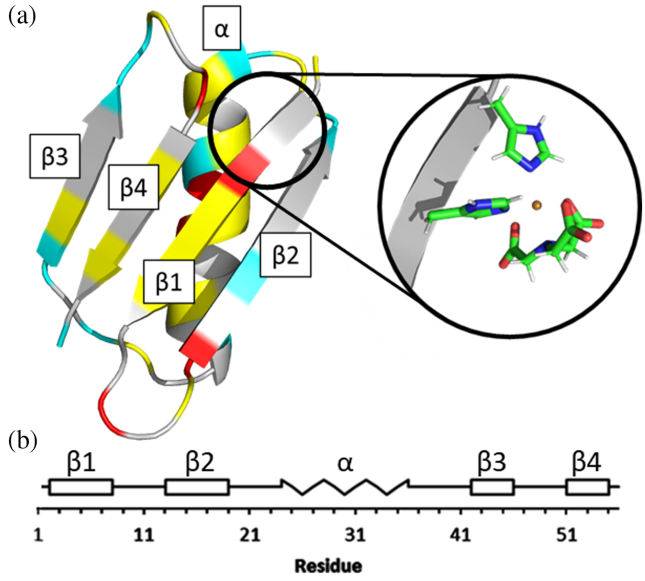

FIGURE 1 (a) The crystal structure of GB1 (PDB: 2QMT). Positively charged amino acids are indicated by red, negatively charged are blue, nonpolar residues are yellow, and polar are gray. Secondary structures β1–4 and the α helix are labeled. The circle displays a Cu(II)NTA-labeled dHis motif positioned on residues i,i + 2 on a β sheet. (b) A schematic of the protein secondary structure. The secondary structural features are displayed as a square (β sheet) and zig-zag (α helix)

In this work, we employ the use of the dHis motif. First, we generated nine GB1 mutants, each containing a single solvent-exposed dHis site. These mutations are located on residues i, i + 2 for β sheet and i, i + 4 for α-helical sites and enable specific coordination to Cu(II)NTA (nitrilotriacetate), demonstrated in Figure 1 with an example β sheet. The dHis mutation results in the Cu(II) atom equatorially binding to two nitrogen from dHis, one nitrogen from NTA, and one oxygen from NTA.[39,57] In addition, the axial ligands are both oxygen from NTA. The dHis positions of the nine GB1 mutants are shown in Figure 2a. Each mutant was labeled with 300 μM Cu(II)NTA to 900 μM GB1. The sub-stoichiometric addition of Cu(II)NTA ensures near 100% binding to protein given reported K_D values.[39,40,46,52] Moreover, we opted to use 3-(N-morpholino)propanesulfonic acid buffer (MOPS) to further improve the labeling efficiency of Cu(II)NTA to dHis.[40]

First, we performed CW-EPR measurements to obtain a library of *g* and hyperfine (hf, *A*) values of Cu(II)NTA bound dHis at sites across the surface of GB1. The *g* and hf values are characteristic for each spin species and provide information on the complexation of the Cu(II)NTA to dHis[58] Therefore, by measuring each site individually, we account for differences in *g* and hf in future simulations as well as identify the range of acceptable values for Cu(II)NTA-labeled dHis in MOPS. Figure 2b shows the CW-EPR spectra obtained for each mutant at 80 K. Each spectrum was simulated using the EasySpin[59] software and the best fit is overlaid on experimental data for each spectrum. We extracted the *g* and hf tensors for each sample from the simulations.

Except for T51H/T53H and T44H/D46H, the CW-EPR spectrum of the other seven mutants consisted of only a single component (cf. Figure 2b). The *g* and hf values are consistent with Cu(II) equatorially coordinated to three nitrogen and one oxygen.[58,60] The CW-EPR spectrum share the characteristic features of Cu(II)NTA coordinated to dHis as indicated by $A_{\|,1}$.[39,40] For T51H/T53H and T44H/D46H, we observed a component with similar *g* and hf values as the other mutants (Component 1) and an additional component with distinct *g* and hf values (Component 2) as made clear in Figure 2c. It is evident that the spectral features of the second component are distinct from those of free Cu(II)NTA as well. Therefore, we can confidently rule out incomplete binding. As such, both these components must represent Cu(II)NTA bound in some way. To further understand the second component in T44H/D46H and T51H/T53H, we obtained more thorough structural analysis from electron spin echo envelope modulation (ESEEM) and circular dichroism (CD). These data are provided in Figures S1 and S2. While ESEEM indicates the dHis is preserved, CD shows that there is a pertubation to the protein structure. Such perturbation is likely due to the short lengths of the β sheets (e.g., five residues of the T51H/T53H and T44H/D46H). Therefore, these two mutants were not used in subsequent CW-EPR analysis.

Figure 3 shows the $g_{\|}$ and $A_{\|}$ values extracted from the simulated spectra as a function of the site location. The values of $g_{\|}$ and $A_{\|}$ values are outlined in Table S1. Interestingly, we observe some variation in $g_{\|}$ values of Component 1. We preclude field instabilities as the source of these differences by using a calibration of quartz signal as described in Table S2 and Figure S3. There are two hypotheses to explain the variation in these values. One explanation is due to changes in local electrostatics. It is known that nitroxide line shapes are sensitive to local protein electrostatics.[61,62] However, there is no direct evidence that shows similar changes with Cu(II)-labeled sites. Even so, $g_{\|}$ of Cu(II) complexes have been reported to decrease in less polar solvents with stronger correlations to a decrease in Lewis basicity.[63,64] The other explanation for these changes in *g* and hyperfine values is that they originate from differences in the lengths and angles of the bonds that chelate the Cu(II)NTA to the dHis site. Prior quantum chemical calculations of $g_{\|}$ in Cu(II)-labeled species have found changes in the magnitude and relative orientation of $g_{\|}$ due to the elasticity of the coordination.[38,42,65,66]

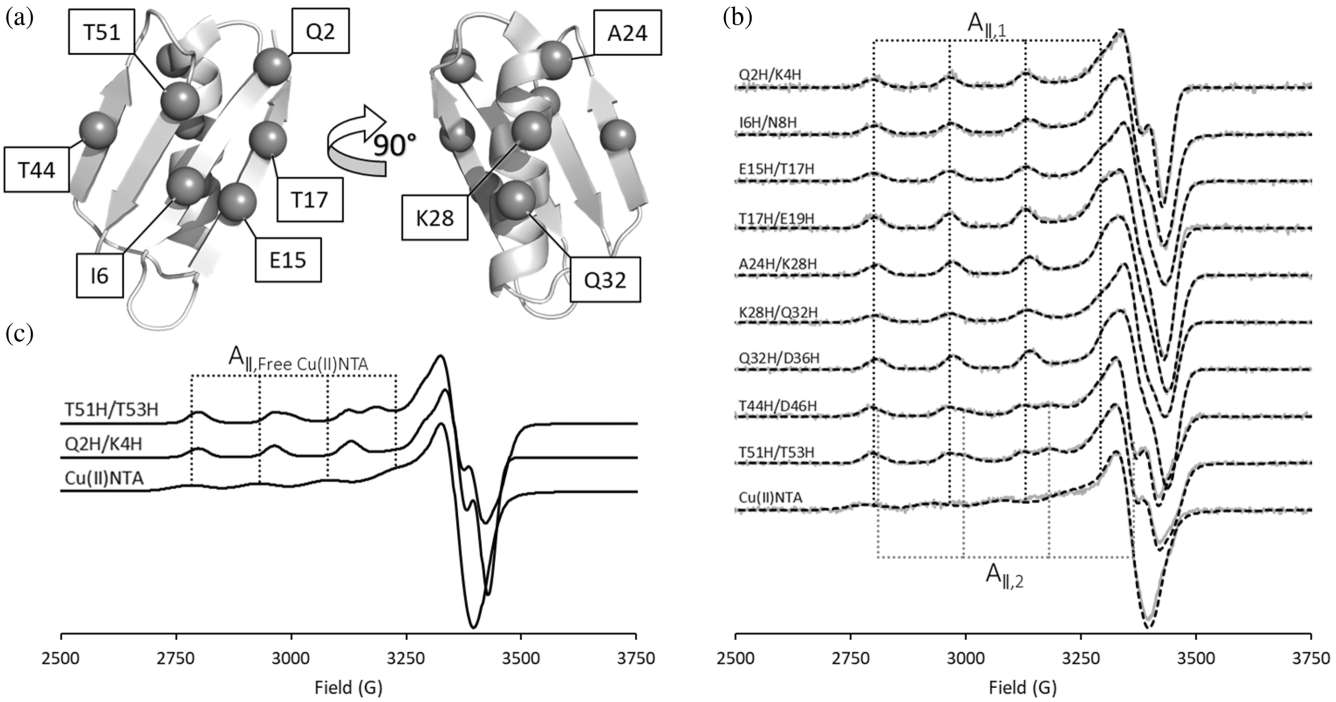

FIGURE 2 (a) Sites of GB1 which were mutated to contain the dHis motif. Note that since dHis requires two histidine mutations, the sphere represents the mutation earlier in the protein sequence. (b) 80 K CW-EPR spectrum of Cu(II)NTA-labeled GB1 (gray) and simulated spectra (black dashed). The spectrum for free Cu(II)NTA is given at the bottom. The $A_{\|}$ splitting is indicated by the vertical dotted lines. $g_{\|}$ is inversely proportional to the field position at the center of the $A_{\|}$ splitting. These values are vital in any future simulation as well as determining successful dHis labeling. (c) The simulated spectra of three unique CW-ESR: T51H/T53H containing two components, Q2H/K4H containing one component consistent with dHis coordination, and free Cu(II)NTA which differs significantly from the other two spectra. The vertical lines represent the $A_{\|}$ splitting of free Cu(II)NTA

Here, residues located near the nonpolar pocket (I6H/N8H, T44H/D46H, T51H/T53H) report lower $g_{\|}$ values than the other mutants. Furthermore, significant changes in $g_{\|}$ values occur when moving across β1 and β2. The largest change between adjacent sites occurs at the I6H/N8H site of β1 located near the hydrophobic core with a $g_{\|}$ 0.004 less than Q2H/K4H surrounded by more polar residues. This results in a 6-G shift at x-band frequencies. On the other hand, we observe only slight changes in the $A_{\|}$ values. The one exception is a 3-G shift for T17H/E19H positioned in close proximity to multiple charged amino acids. With these $g_{\|}$ and $A_{\|}$ values, appropriate analysis of subsequent EPR measurements is possible. Additionally, the use of higher frequency experiments would further increase the precision of $g_{\|}$ and $A_{\|}$ determination.[67]

2.2 | CW-EPR spectra at ambient temperature

Next, we obtained the CW-EPR spectra of each Cu(II)NTA-labeled GB1 mutant at 291 K to measure site-specific dynamics. The data are shown in Figure 4. These samples contained 900 μM GB1-labeled with 300 μM Cu(II)NTA with 20% Ficoll in MOPs buffer. The addition of Ficoll slows the global protein tumbling to minimize its influence on the CW-EPR spectra.[68] These experiments took *ca*. 12 hr to run. However, the experimental time can be reduced to 1 hr by using equimolar Cu(II)NTA to dHis concentrations rather than sub-stoichiometric amounts, as shown in Figure S4. Thus, this technique is limited to proteins which either can tolerate higher concentrations for 1 hr or are stable for *ca*. 12 hr at 300 μM.

As shown in Figure 4, a visual examination shows changes in the peak-to-peak splitting of the CW-EPR spectrum for the series, most evident from the high field line marked with an asterisk. In each case, the splitting differs from the low-temperature data due to averaging of *g* and hf tensor from residue-specific reorientational dynamics.

To qualitatively compare the dynamics of each mutant, we define ΔA as the difference between the $A_{\|}$ peak splitting, as shown in Figure 2b, and the partially averaged peak-to-peak separation, A_{δ},[48] observed in

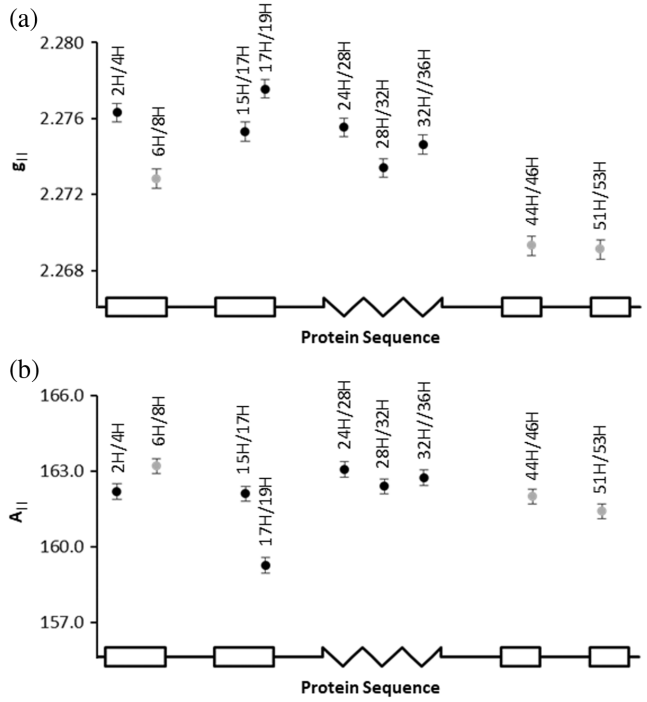

FIGURE 3 Plots of (a) $g_{||}$ and (b) $A_{||}$ values as a function of residue number are shown. The gray dots represent residues located near the nonpolar pocket of GB1, whereas the black dots represent residues located elsewhere. The secondary structural features are displayed as a square (β sheet) and zig-zag (α helix) at the bottom. Because each mutation involves two residues, the residue number plotted is the average of the two (e.g., Q2H/K4H will be positioned at residue 3). Mutant T44H/D46H and T51H/T53H have two components, but only Component 1 is shown

Figure 4. Including $A_{||}$ in the definition of ΔA accounts for the subtle differences due to local electrostatics and/or coordination. In this definition, a ΔA value of 0 implies that the dynamics is frozen on the EPR timescale. On the other hand, a larger value of ΔA would correlate with faster dynamics. These values of ΔA for all mutants are outlined in Table 1. Utilizing these values serve as a simplified way to quantitatively compare the dynamics between two different sites within a protein.

Data on the I6H/N8H, E15H/T17H, and K28H/Q32H mutants were previously published in Tris buffer.[48] However, we opted to use MOPS buffer as it allows for better binding of Cu(II)NTA to dHis.[40] In previous work, I6H/N8H showed the fastest dynamics, while the dynamics of E15H/T17H and K28H/Q32H were indistinguishable. We observed the same trend in MOPS. The ΔA of I6H/N8H, E15H/T17H, and K28H/Q32H were 14 ± 2, 8 ± 2, and 10 ± 2 G, respectively. Furthermore, the ΔA of A24H/K28H was notably higher at 20 ± 2 G. This observation for A24H/K28H is consistent with prior results from NMR that report A24 to be more flexible as it is located in the first N-terminal turn of the α helix before the helix can form strong hydrogen bonds with the rest of the protein.[51] Another residue reporting faster dynamics is T17H/E19H with a ΔA of 12 ± 2 G. This dHis motif resides at the C-terminal end of β2 where no involvement in hydrogen bonding occurs.[49]

While ΔA provides a method to qualitatively compare CW-EPR data, we simulated the data using slow motional theory[69] in order to obtain quantitative

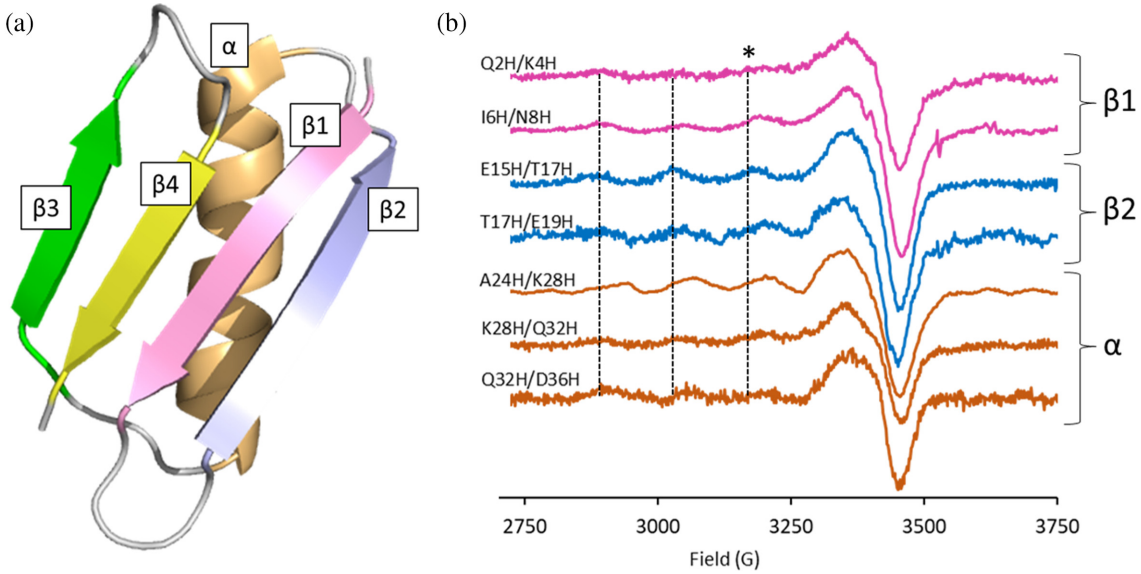

FIGURE 4 (a) The crystal structure of GB1 (pdb: 2QMT) with labeled secondary structure. (b) CW-EPR spectra of Cu(II)NTA-labeled GB1 mutants at 291 K. The secondary structure in which the site resides is reported next to their respective spectrum. The vertical dotted lines represent the A_S for Q2H/K4H and serve as a visual comparison to the A_S of the other mutants

Secondary structure	Mutant	$A_{\parallel}$ (G)	A_{δ} (G)	Δ:A (G)
β1	Q2H/K4H	162.2 ± 0.3	152 ± 2	10 ± 2
β1	I6H/N8H	163.2 ± 0.3	149 ± 2	14 ± 2
β2	E15H/T17H	162.1 ± 0.3	154 ± 2	8 ± 2
β2	T17H/E19H	159.3 ± 0.3	147 ± 2	12 ± 2
α	A24H/K28H	163.1 ± 0.3	143 ± 2	20 ± 2
α	K28H/Q32H	162.4 ± 0.3	152 ± 2	10 ± 2
α	Q32H/D36H	162.7 ± 0.3	149 ± 3	14 ± 3

TABLE 1 ΔA values calculated from the difference between $A_{\parallel}$ and A_{δ}

information and remove biases in the estimation of peak splitting. For room temperature simulations, we used the g and hf tensors that were measured at 80 K (cf. Figure 2b). For these Cu(II) simulations, we tried a variety of approaches. First, we found that the microscopic order macroscopic disorder (MOMD), which is typically used for nitroxide-labeled proteins,[70] is not necessary for the Cu(II)–EPR simulations. Details are provided in Figures S5–S7. Satisfactory fits were obtained by considering isotropic reorientation, anisotropic line broadening, and the rotational diffusion rate (R), related to the rotational correlation time (τ_R) as shown in Equation 1.[71,72]

$$R = (6\tau_R)^{-1} \quad (1)$$

The simulated CW-EPR spectra are shown in Figure 5. Here, residues with a smaller rotational correlation time are considered to have faster dynamics. These results are consistent with the ΔA analysis discussed earlier. Residues I6H/N8H, T17H/E19H, A24H/K28H, and Q32H/D36H underwent the fastest motion with τ_R equal to 0.87 ± 0.09, 0.84 ± 0.09, 0.60 ± 0.09, and 0.86 ± 0.11 ns, respectively. It is also noteworthy that residues closer to the middle of a secondary structure, E15H/T17H and K28H/Q32H, have slower dynamics, that is, higher τ_R, 1.20 ± 0.12 and 1.06 ± 0.11 ns, respectively. NMR results also notice a similar trend in which residues at the middle of GB1 have higher order parameters than residues at either terminal end of the secondary structure.[73] More importantly, we observe subtle changes in dynamics within secondary structures. Site Q2H/K4H had fluctuations around 0.4 ns slower than I6H/N8H, despite both positioned at the edge of β1. The sites along the α helix showcase a similar trend. Both A24H/K28H and Q32H/D36H have faster dynamics than K28H/Q32H positioned at the middle of the helix. However, there are measurable differences between the two edge mutants. Here, A24H/K28H fluctuations occur roughly 0.26 ns faster than

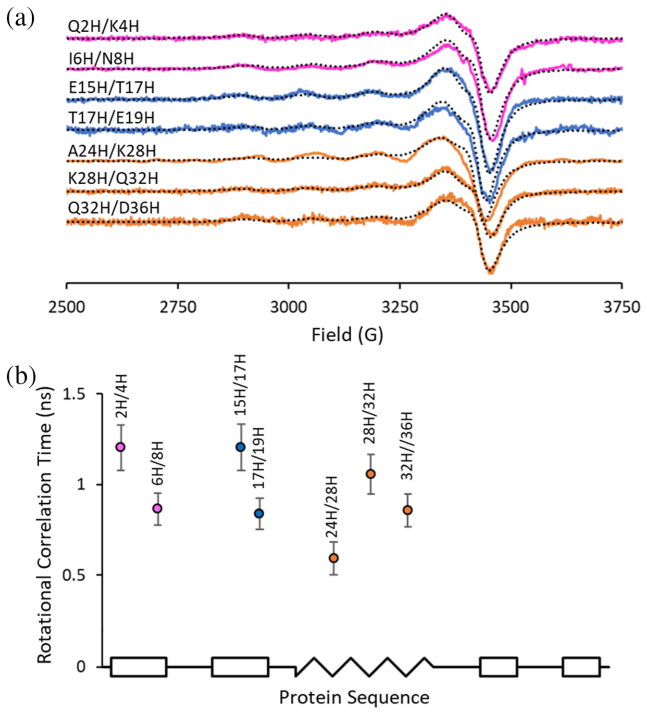

FIGURE 5 (a) The simulated CW-EPR spectra (black dotted) overlayed onto the respective experimental data (gray). (b) Simulated rotational diffusion rates for each simulated CW-EPR spectra

Q32H/D36H. A24 is known to be more flexible as it does not form strong hydrogen bonds with the rest of the protein, whereas Q32 and D36 are positioned closer to the hydrophobic core and has internal hydrogen bonding.[51,74] Note that the 0.2 ns difference in correlation time between Cu(II)NTA spectra results in easily distinguishable ΔA. Similar changes in R1 would result in subtle differences in peak broadening and are more difficult to observe.[75,76] The exact rotational correlation times are listed in Table S3. Additionally, a comparison to the ΔA values is shown in Figure S8. We anticipate that this technique is applicable from a 30-ns to 50-ps timescale.[48]

2.3 | MD simulations and comparison to simulated EPR spectra

To further investigate the site-specific dynamics of GB1, 200 ns molecular dynamics (MD) simulations were acquired for each of the mutants to monitor the motion of the Cu(II) atom. The MD simulations explicitly included the Cu(II)-NTA label using force fields that were developed recently.[38] Figure 6a shows the MD results for the Cu(II)NTA-labeled Q2H/K4H mutant. Results for the rest of the mutants are shown in Figure S9. The protein during each frame of the MD simulation was aligned by its secondary structure. This eliminates the global tumbling and allows selective observation of residue-specific motion. Notably, the Cu(II) atom occupies a small range of space relative to other spin labels, consistent with previous MD work[38] and confirms the rigidity of Cu(II)NTA chelation to dHis. In order to analyze the MD for comparison with EPR, we first need the relative orientation between $g_{||}$ and the applied magnetic field, assumed to be the z direction defined in Figure 6a, for each MD frame. Due to the axial symmetry of the d_{z^2} orbital, that is, the orbital containing the unpaired electron, a fluctuation about $g_{||}$ will not change the resulting CW-EPR spectrum. Therefore, Cu(II) is only sensitive to the fluctuations around the *x*-axis or *y*-axis. Since the N atom of histidine coordinates equatorially, that is, the axial axis, $g_{||}$ was approximated as the vector, $\vec{r}$, defined as the cross product of the two Cu(II)-N vectors, $\vec{N(1)} \times \vec{N(2)}$. Furthermore, this vector was used to obtain an angle versus time plot as shown in Figure 6b,c. The angles, θ (polar angle) and ϕ (azimuthal

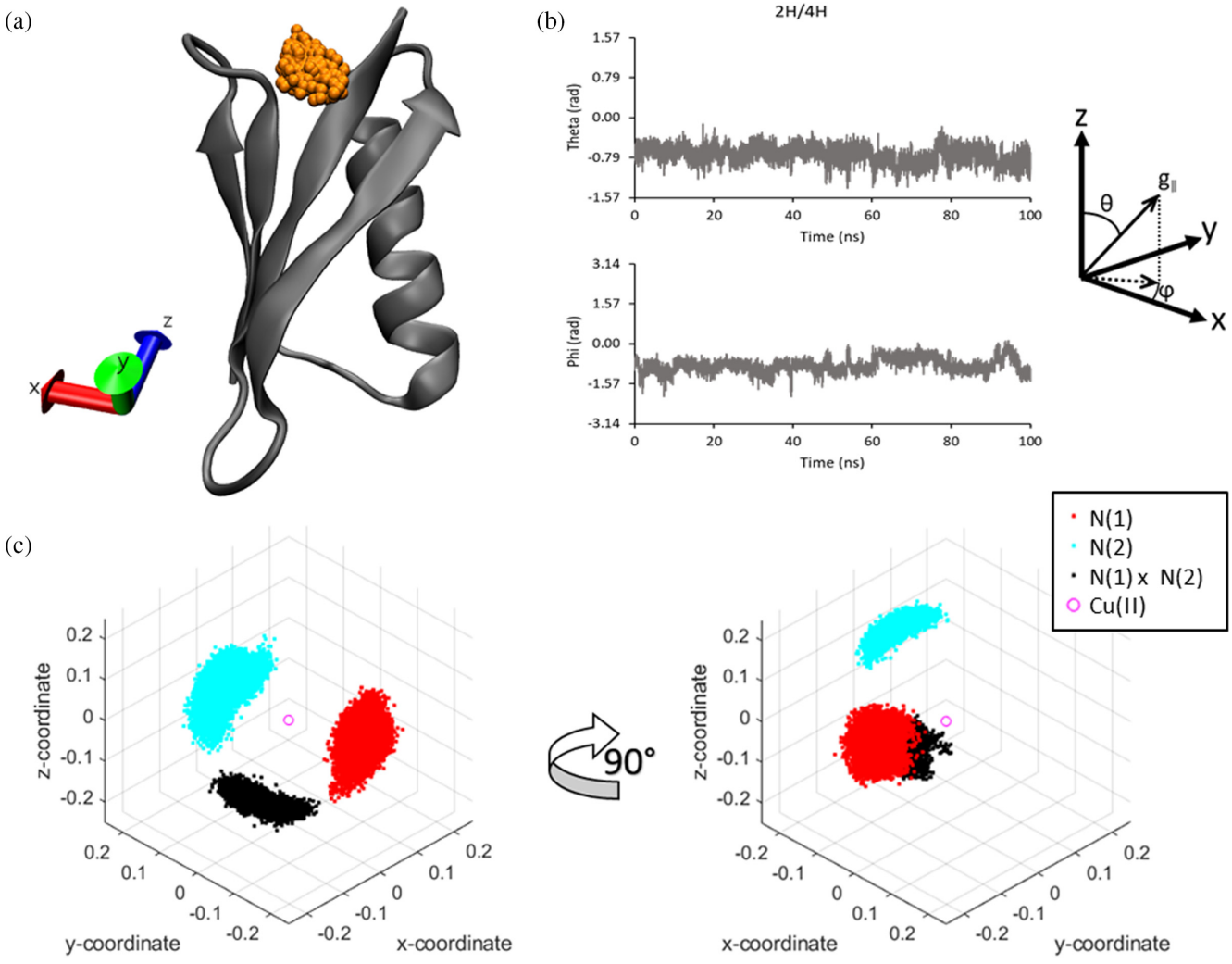

FIGURE 6 (a) Averaged structure of Q2H/K4H GB1 from the 200 ns MD simulation. Position of the Cu(II) atom throughout the Q2H/K4H MD simulation is represented by the orange spheres. (b) θ (polar angle) and ϕ (azimuthal angle) values of $\vec{N(1)} \times \vec{N(2)}$ throughout the course of the MD simulation. (c) The vectors connecting the Cu(II) atom (purple circle) and the coordinated N atoms from dHis (red and blue dots) are shown. In order to approximate the z direction, the cross product of the two Cu-N vectors was also obtained (black dots)

angle), are defined in Figure 6b. From this, we can calculate the tumbling time from MD.

To compare between the MD data and CW-EPR spectra, the autocorrelation functions[71] were calculated for the orientation of $N(1) \times N(2)$ from the MD simulations (Figures 7a and S10). The general autocorrelation function $g(\tau)$ of a function $\vec{r}\,(t)$ is defined as:

$$g(\tau) = < \left[\vec{r}\,(t) - \overline{r} \right] \cdot \left[\vec{r}\,(t+\tau) - \overline{r} \right] > \quad (2)$$

$$\overline{r} = < \vec{r}\,(t) > \quad (3)$$

where τ represents the lag time and the angular brackets indicate the average value of the function. In our case, the function describes how the averaged orientation of $N(1) \times N(2)$ across each frame of the MD simulation correlates with the initial orientation.[77,78] When τ is equal to t, the autocorrelation value is 1 since the averaged orientation is exactly the same as the initial orientation. As the MD simulation continues, the averaged orientation of $N(1) \times N(2)$ shifts away from the initial orientation. Eventually, the averaged orientation will lose its correlation with the original orientation and the autocorrelation will reach a baseline. For our context, the decay rate of the autocorrelation function quantifies the internal motions of $N(1) \times N(2)$ throughout the MD simulation. Overall, fast and large motions have autocorrelation functions that decay faster than rigid and slow motions. The resulting autocorrelation functions were fit to a biexponential decay. The faster component had an autocorrelation time of 10–15 ps. Since the MD simulation had a step size of 10 ps, these are likely due to motions faster than the MD step size, such as vibrational motions. The longer autocorrelation time, τ_R, relates to the tumbling of the Cu(II) $g_{||}$ relative to the applied magnetic field. Figure 7b compares the MD τ_R to the EPR τ_R. Exact values are in Table S3. Additionally, the CW-EPR spectra were fit using the τ_R determined from the MD autocorrelation fit, as shown in Figure S11. Here, when MD-derived τ_R was close to the EPR τ_R, we found reasonable spectral simulations. In two cases, T17H/E19H and A24H/K28H, simulations inadequately fit the EPR data. Note that MD is not expected to perfectly predict the correlation times observed from EPR since MD does not include buffer molecules, sampling may be incomplete, and the force field parameters may be imperfect. However, we expect consistent trends between the two techniques. Indeed, we found that sites with shorter correlation times from EPR, such as T17H/E19H and A24H/K28H, showed faster dynamics in MD. Likewise, sites with slower dynamics such as Q2H/K4H, E15H/T17H, and K28H/Q32H had longer τ_R from MD. Consequently, the correlation between MD and EPR τ_R supports that the EPR analysis does reflect the local dynamics.

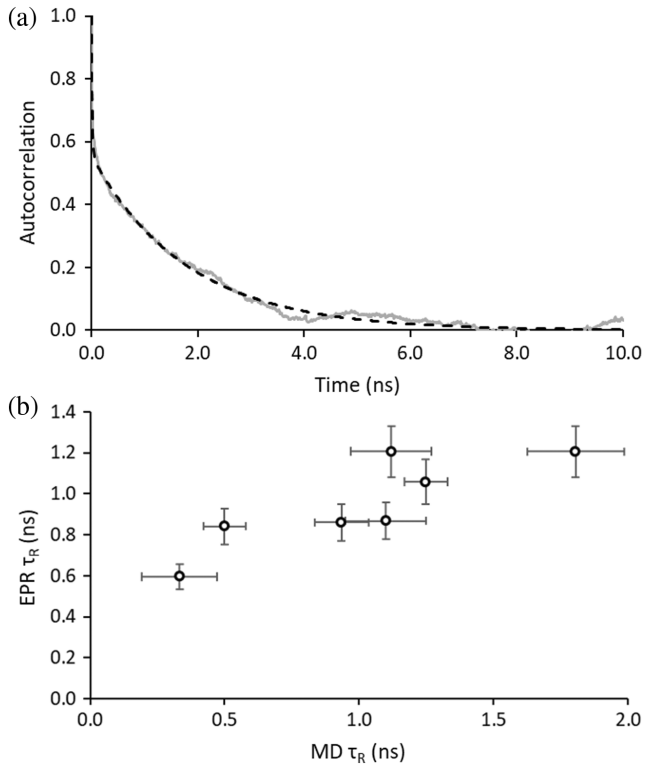

FIGURE 7 (a) Autocorrelation function from MD of Q2H/K4H (gray solid) fit using a biexponential decay (black dashed). (b) Rotational correlation times obtained from simulated CW-EPR spectra compared to the autocorrelation time obtained from MD simulations. The dashed diagonal line represents a 1:1 relationship between the two correlation times

3 | CONCLUSION

In this work, we have shown the utility of the rigid dHis motif to obtain information other than distance constraints. First, we showed that the $g_{||}$ and $A_{||}$ values of Cu(II)NTA bound to dHis subtly change for different mutants. Then using these values, we outlined the use of the dHis motif to understand site-specific dynamics. Measurement of spectral shifts from the frozen spectra (i.e., ΔA) of room temperature CW-EPR spectra provides a simple, qualitative analysis of site-specific dynamics that requires little to no complex simulations of the EPR results. However, simulations further quantify these changes and show good agreement with our MD results as well as provide consistent information to previously published work on GB1. We show that due to large anisotropy of the Cu(II) g and hyperfine values even very small changes in dynamics lead to distinguishable

changes in the room temperature data. Finally, the dHis motif can allow for EPR on cysteine-rich proteins as standard cysteine-based labels usually require other native cysteine residues to be mutated out. Notably, we show here that the dHis methodology is applicable to both helical and sheet sites. However, these experiments require the protein to be stable either for a longer duration or at a higher protein concentration than necessary with R1-labeled systems. Nonetheless, the benefits of Cu(II) NTA labeling of dHis provide another avenue to understand protein structure and dynamics.

4 | MATERIALS AND METHODS

4.1 | Sample preparation

Cu(II)NTA synthesis and labeling was performed following previously published work.[39,40,42] A step-by-step protocol has also been published recently.[79] GB1 expression and purification were performed as described previously.[28,29] All EPR samples contained GB1 underloaded with Cu(II)NTA to ensure near 100% binding. These samples contained a final 300 μM Cu(II)NTA and 900 μM GB1 in 50 mM MOPs buffer (pH = 7.4). MOPs were chosen as it resulted in the highest labeling efficiency in previous work.[40] Samples prepared for 80 K CW-EPR spectra and ESEEM contained 20% v/v glycerol in a total of 120 μL. Glycerol serves as a cryoprotectant to prevent the EPR tube from shattering. Samples were placed in 3 mm I.D. × 4 mm O.D. quartz tubes, immediately flash frozen in liquefied MAPP gas, and stored in the −80°C freezer until ready for use. Samples prepared for 291 K CW-EPR contained 20% w/v Ficoll. Approximately 40 μL was drawn into quartz capillary tubes (0.8 mm I.D. × 1.0 mm O.D.) and was run immediately.

4.2 | EPR measurements and analysis

EPR experiments were performed on a Bruker ElexSys E680 CW/FT X-band spectrometer. Spectra (80 K) were obtained using a Bruker ER4118-MD5 resonator, Oxford ITC503 temperature controller, Oxford CF935 dynamic continuous-flow cryostat, and Oxford LLT 650 low loss transfer tube. CW-EPR parameters were: center field = 3,100 G, sweep width = 2,000 G, microwave frequency = ~9.68 GHz, modulation amplitude = 4 G, modulation frequency = 100 kHz, conversion time = 20.48 ms, number of scans = 20, number of points = 1,024. Experiments at ambient temperature were performed in a Bruker ER4122 SHQE-W1 high-resolution resonator. Ambient temperature was 291 ± 1 K. CW-EPR parameters were: center field = 3,200 G, sweep width = 1,600 G, microwave frequency = ~9.87 GHz, modulation amplitude = 6 G, modulation frequency = 100 kHz, conversion time = 20.48 ms, number of points = 1,024. The spectra were acquired for 12 hr each (approximately 2,000–4,000 scans).

The g and A values of each sample were determined by simulating the 80 K CW-EPR spectra in EasySpin using the pepper function.[59] The $g_{\|}$ and $A_{\|}$ values are outlined in Table S1. CW-EPR spectra (291 K) were simulated using NLSL MOMD.[69] Data were fit by only varying the rotational diffusion rate, RBAR, and the line width (WPRP and WPLL).

Three-pulse ESEEM experiments were performed at 80 K.[80] The pulse sequence used is as follows: π/2 – t – π/2 – T – π/2 – echo. The parameters are as follows: π/2 = 6 ns, t = 142 ns, T = 288 ns and was incremented in steps of 16 ns. ESEEM experiments were obtained at the magnetic field with the highest intensity signal. Four-step phase cycling was implemented to filter out unwanted echos.[81] The resulting time domain signal was fit to a stretched exponential decay for background subtraction. Finally, the time domain signal was Fourier transformed using the Bruker XEPR software.

4.3 | MD simulations and processing of MD trajectories

MD simulations with appropriate Cu(II)NTA force fields were obtained following previous work.[38,48] Autocorrelation times were processed using python scripts provided by Prof. Nikolai Skrynnikov and Sergei Izmailov, similar to pyxmolpp2.[77,82] The autocorrelation functions were fit to a biexponential decay. Errors were obtained by calculating the range of τ_R values which resulted in a minimum RMSD.

4.4 | Circular dichroism

CD data on T51H/T53H and T44H/D46H GB1 were acquired using an Olis 17 UV/Vis//NIR spectrophotometer. Samples contained 40 μM protein in 50 mM MOPS buffer at pH = 7.4. CD scans were obtained at 25°C from 200 to 260 nm. The temperature melt was acquired at a 220-nm wavelength with a 2-minute equilibration period between each temperature point. Each temperature during the melt was subsequently background subtracted using the molar ellipticity at 260 nm. Once finished, the temperature was set back to 25°C to test protein refolding.

AUTHOR CONTRIBUTIONS

Kevin Singewald: Conceptualization (supporting); data curation (lead); formal analysis (lead); investigation (lead); software (equal); validation (lead); visualization (lead); writing – original draft (equal); writing – review and editing (equal). **James Wilkinson:** Data curation (supporting); investigation (supporting); software (supporting); validation (supporting); writing – original draft (supporting); writing – review and editing (supporting). **Zikri Hasanbasri:** Formal analysis (supporting); investigation (supporting); methodology (supporting); software (equal); writing – original draft (supporting); writing – review and editing (supporting). **Sunil Saxena:** Conceptualization (lead); formal analysis (supporting); funding acquisition (lead); project administration (lead); supervision (lead); writing – original draft (equal); writing – review and editing (equal).

ACKNOWLEDGMENTS

This research was supported by the National Science Foundation (NSF BSF MCB-2006154). MD simulations were performed at the University of Pittsburgh's Center for Research Computing. Nikolai Skrynnikov and Sergei Izmailov are thanked for providing the software to extract autocorrelation times from MD.

CONFLICT OF INTEREST

The authors declare no competing interests.

ORCID

Sunil Saxena https://orcid.org/0000-0001-9098-6114

REFERENCES

1. Bilej M. Cellular defense mechanisms. Immunology of annelids. Florida: CRC Press, 1994; p. 168–200.
2. Hammes-Schiffer S, Benkovic SJ. Relating protein motion to catalysis. Annu Rev Biochem. 2006;75:519–541.
3. Rothman JE. Mechanisms of intracellular protein transport. Nature. 1994;372(6501):55–63.
4. Yang L-Q, Sang P, Tao Y, et al. Protein dynamics and motions in relation to their functions: Several case studies and the underlying mechanisms. J Biomol Struct Dyn. 2014;32(3):372–393.
5. Smith J, Kuczera K, Karplus M. Dynamics of myoglobin: Comparison of simulation results with neutron scattering spectra. Proc Natl Acad Sci. 1990;87(4):1601–1605.
6. Henzler-Wildman KA, Thai V, Lei M, et al. Intrinsic motions along an enzymatic reaction trajectory. Nature. 2007;450(7171):838–844.
7. Yu L, Wang W, Ling S, et al. CW-EPR studies revealed different motional properties and oligomeric states of the integrin β1a transmembrane domain in detergent micelles or liposomes. Sci Rep. 2015;5(1):7848.
8. Lawless MJ, Pettersson JR, Rule GS, Lanni F, Saxena S. ESR resolves the C terminus structure of the ligand-free human glutathione S-transferase A1-1. Biophys J. 2018;114(3):592–601.
9. McHaourab HS, Oh KJ, Fang CJ, Hubbell WL. Conformation of T4 lysozyme in solution. Hinge-bending motion and the substrate-induced conformational transition studied by site-directed spin labeling. Biochemistry. 1997;36(2):307–316.
10. Boehr DD, Dyson HJ, Wright PE. An NMR perspective on enzyme dynamics. Chem Rev. 2006;106(8):3055–3079.
11. Roberts GC. NMR spectroscopy in structure-based drug design. Curr Opin Biotechnol. 1999;10(1):42–47.
12. Belcher Dufrisne M, Swope N, Kieber M, et al. Human CEACAM1 N-domain dimerization is independent from glycan modifications. Structure. 2022;30:658–670.e5.
13. Weickert S, Wawrzyniuk M, John L, Rüdiger SG, Drescher M. The mechanism of Hsp90-induced oligomerizaton of tau. Sci Adv. 2020;6(11):eaax6999.
14. Liu Z, Huang X, Hu L, et al. Effects of hinge-region natural polymorphisms on human immunodeficiency virus-type 1 protease structure, dynamics, and drug pressure evolution. J Biol Chem. 2016;291(43):22741–22756.
15. Ishima R, Torchia DA. Protein dynamics from NMR. Nat Struct Biol. 2000;7(9):740–743.
16. Wüthrich K. The second decade—Into the third millenium. Nat Struct Biol. 1998;5(7):492–495.
17. Tugarinov V, Muhandiram R, Ayed A, Kay LE. Four-dimensional NMR spectroscopy of a 723-residue protein: Chemical shift assignments and secondary structure of malate synthase g. J Am Chem Soc. 2002;124(34):10025–10035.
18. Sanders CR, Sönnichsen F. Solution NMR of membrane proteins: Practice and challenges. Magn Reson Chem. 2006;44(S1):S24–S40.
19. Toyama Y, Kay LE. Probing allosteric interactions in homo-oligomeric molecular machines using solution NMR spectroscopy. Proc Natl Acad Sci. 2021;118(50):e2116325118.
20. van Doorslaer S, Jeschke G. Dynamics by EPR: Picosecond to microsecond time scales. Fluxional Organometallic and Coordination Compounds. Germany: Wiley, 2005; p. 6.219–6.242.
21. Lewandowski JR, Halse ME, Blackledge M, Emsley L. Direct observation of hierarchical protein dynamics. Science. 2015;348(6234):578–581.
22. Hubbell WL, López CJ, Altenbach C, Yang Z. Technological advances in site-directed spin labeling of proteins. Curr Opin Struct Biol. 2013;23(5):725–733.
23. Berliner LJ, Grunwald J, Hankovszky HO, Hideg K. A novel reversible thiol-specific spin label: Papain active site labeling and inhibition. Anal Biochem. 1982;119(2):450–455.
24. Todd AP, Cong J, Levinthal F, Levinthal C, Hubell WL. Site-directed mutagenesis of colicin E1 provides specific attachment sites for spin labels whose spectra are sensitive to local conformation. Proteins: Struct Funct Bioinform. 1989;6(3):294–305.
25. Mchaourab HS, Lietzow MA, Hideg K, Hubbell WL. Motion of spin-labeled side chains in T4 lysozyme. Correlation with protein structure and dynamics. Biochemistry. 1996;35(24):7692–7704.
26. Fleissner MR, Cascio D, Hubbell WL. Structural origin of weakly ordered nitroxide motion in spin-labeled proteins. Protein Sci. 2009;18(5):893–908.
27. Columbus L, Kálai T, Jekö J, Hideg K, Hubbell WL. Molecular motion of spin labeled side chains in α-helices: Analysis by variation of side chain structure. Biochemistry. 2001;40(13):3828–3846.

28. Cunningham TF, Pornsuwan S, Horne WS, Saxena S. Rotameric preferences of a protein spin label at edge-strand β-sheet sites. Protein Sci. 2016;25(5):1049–1060.
29. Cunningham TF, McGoff MS, Sengupta I, Jaroniec CP, Horne WS, Saxena S. High-resolution structure of a protein spin-label in a solvent-exposed β-sheet and comparison with DEER spectroscopy. Biochemistry. 2012;51(32):6350–6359.
30. Lietzow MA, Hubbell WL. Motion of spin label side chains in cellular retinol-binding protein: Correlation with structure and nearest-neighbor interactions in an antiparallel β-sheet. Biochemistry. 2004;43(11):3137–3151.
31. Freed DM, Khan AK, Horanyi PS, Cafiso DS. Molecular origin of electron paramagnetic resonance line shapes on β-barrel membrane proteins: The local solvation environment modulates spin-label configuration. Biochemistry. 2011;50(41):8792–8803.
32. Lösel RM, Philipp R, Kálai T, Hideg K, Trommer WE. Synthesis and application of novel bifunctional spin labels. Bioconjug Chem. 1999;10(4):578–582.
33. Thompson AR, Binder BP, McCaffrey JE, Svensson B, Thomas DD. Bifunctional spin labeling of muscle proteins: Accurate rotational dynamics, orientation, and distance by EPR. Methods in enzymology. Volume 564. Cambridge, MA: Academic Press, 2015; p. 101–123.
34. Fleissner MR, Bridges MD, Brooks EK, et al. Structure and dynamics of a conformationally constrained nitroxide side chain and applications in EPR spectroscopy. Proc Natl Acad Sci. 2011;108(39):16241–16246.
35. Poole LB. The basics of thiols and cysteines in redox biology and chemistry. Free Radic Biol Med. 2015;80:148–157.
36. Qiu H, Honey DM, Kingsbury JS, et al. Impact of cysteine variants on the structure, activity, and stability of recombinant human α-galactosidase a. Protein Sci. 2015;24(9):1401–1411.
37. Cunningham TF, Putterman MR, Desai A, Horne WS, Saxena S. The double-histidine Cu2+-binding motif: A highly rigid, site-specific spin probe for electron spin resonance distance measurements. Angewandte Chemie. 2015;127(21):6428–6432.
38. Bogetti X, Ghosh S, Gamble Jarvi A, Wang J, Saxena S. Molecular dynamics simulations based on newly developed force field parameters for Cu2+ spin labels provide insights into double histidine-based double electron-electron resonance. J Phys Chem B. 2020;124:2788–2797.
39. Ghosh S, Lawless MJ, Rule GS, Saxena S. The Cu2+−nitrilotriacetic acid complex improves loading of α-helical double histidine site for precise distance measurements by pulsed ESR. J Magn Reson. 2018;286:163–171.
40. Gamble Jarvi A, Casto J, Saxena S. Buffer effects on site directed Cu2+−labeling using the double histidine motif. J Magn Reson. 2020;320:106848.
41. Wort JL, Arya S, Ackermann K, Stewart AJ, Bode BE. Pulse dipolar EPR reveals double-histidine motif CuII–NTA spin-labeling robustness against competitor ions. J Phys Chem Lett. 2021;12(11):2815–2819.
42. Gamble Jarvi A, Bogetti X, Singewald K, Ghosh S, Saxena S. Going the dHis-tance: Site-directed Cu2+ labeling of proteins and nucleic acids. Acc Chem Res. 2021;54(6):1481–1491.
43. Gamble Jarvi A, Cunningham TF, Saxena S. Efficient localization of a native metal ion within a protein by cu 2+−based EPR distance measurements. Phys Chem Chem Phys. 2019; 21(20):10238–10243.
44. Sameach H, Ghosh S, Gevorkyan-Airapetov L, Saxena S, Ruthstein S. Inside cover: EPR spectroscopy detects various active state conformations of the transcriptional regulator CueR (Angew. Chem. Int. Ed. 10/2019). Angew Chem Int Ed. 2019;58(10):2908.
45. Gamble Jarvi A, Ranguelova K, Ghosh S, Weber RT, Saxena S. On the use of Q-band double electron–electron resonance to resolve the relative orientations of two double histidine-bound Cu2+ ions in a protein. J Phys Chem B. 2018;122(47):10669–10677.
46. Wort JL, Ackermann K, Giannoulis A, Stewart AJ, Norman DG, Bode BE. Sub-micromolar pulse dipolar EPR spectroscopy reveals increasing CuII-labelling of double-histidine motifs with lower temperature. Angewandte Chemie. 2019;131(34):11807–11811.
47. Ackermann K, Wort JL, Bode BE. Nanomolar pulse dipolar EPR spectroscopy in proteins: CuII–CuII and Nitroxide–Nitroxide cases. J Phys Chem B. 2021;125(20):5358–5364.
48. Singewald K, Bogetti X, Sinha K, Rule GS, Saxena S. Double histidine based EPR measurements at physiological temperatures permit site-specific elucidation of hidden dynamics in enzymes. Angewandte Chemie. 2020;132(51):23240–23244.
49. Shi X, Rienstra CM. Site-specific internal motions in GB1 protein microcrystals revealed by 3D 2H–13C–13C solid-state NMR spectroscopy. J Am Chem Soc. 2016;138(12):4105–4119.
50. Sheppard D, Li D-W, Brüschweiler R, Tugarinov V. Deuterium spin probes of backbone order in proteins: 2H NMR relaxation study of deuterated carbon α sites. J Am Chem Soc. 2009; 131(43):15853–15865.
51. Idiyatullin D, Daragan VA, Mayo KH. 15NH backbone dynamics of protein GB1: Comparison of order parameters and correlation times derived using various "model-free" approaches. J Phys Chem B. 2003;107(11):2602–2609.
52. Lawless MJ, Ghosh S, Cunningham TF, Shimshi A, Saxena S. On the use of the cu 2+−iminodiacetic acid complex for double histidine based distance measurements by pulsed ESR. Phys Chem Chem Phys. 2017;19(31):20959–20967.
53. Casto J, Mandato A, Saxena S. dHis-troying barriers: Deuteration provides a pathway to increase sensitivity and accessible distances for Cu2+ labels. J Phys Chem Lett. 2021;12(19):4681–4685.
54. Izmailov SA, Rabdano SO, Hasanbasri Z, Podkorytov IS, Saxena S, Skrynnikov NR. Structural and dynamic origins of ESR lineshapes in spin-labeled GB1 domain: The insights from spin dynamics simulations based on long MD trajectories. Sci Rep. 2020;10(1):1–18.
55. Frericks Schmidt HL, Sperling LJ, Gao YG, et al. Crystal polymorphism of protein GB1 examined by solid-state NMR spectroscopy and X-ray diffraction. J Phys Chem B. 2007;111(51): 14362–14369.
56. Berggård T, Julenius K, Ogard A, Drakenberg T, Linse S. Fragment complementation studies of protein stabilization by hydrophobic core residues. Biochemistry. 2001;40(5):1257–1264.
57. Stadlbauer S, Riechers A, Späth A, König B. Utilizing reversible copper (II) peptide coordination in a sequence-selective luminescent receptor. Chem A Eur J. 2008;14(8):2536–2541.
58. Peisach J, Blumberg W. Structural implications derived from the analysis of electron paramagnetic resonance spectra of

natural and artificial copper proteins. Arch Biochem Biophys. 1974;165(2):691–708.
59. Stoll S, Schweiger A. EasySpin, a comprehensive software package for spectral simulation and analysis in EPR. J Magn Reson. 2006;178(1):42–55.
60. Silva KI, Michael BC, Geib SJ, Saxena S. ESEEM analysis of multi-histidine cu(II)-coordination in model complexes, peptides, and amyloid-β. J Phys Chem B. 2014;118(30):8935–8944.
61. Voinov MA, Ruuge A, Reznikov VA, Grigor'ev IA, Smirnov AI. Mapping local protein electrostatics by EPR of pH-sensitive thiol-specific nitroxide. Biochemistry. 2008;47(20):5626–5637.
62. Smirnov AI, Ruuge A, Reznikov VA, Voinov MA, Grigor'ev IA. Site-directed electrostatic measurements with a thiol-specific pH-sensitive Nitroxide: Differentiating local p K and polarity effects by high-field EPR. J Am Chem Soc. 2004;126(29):8872–8873.
63. Garribba E, Micera G, Sanna D, Strinna-Erre L. The Cu(II)-2,2′-bipyridine system revisited. Inorg Chim Acta. 2000;299(2):253–261.
64. Tateaki O, Tadashi F, Nobuyuki T, Hiroshi Y. Solvent effects on the ESR spectra of copper(II) complexes. A consideration of the donicity of water and methanol. Bull Chem Soc Jpn. 1976;49(10):2759–2761.
65. Gamble Jarvi A, Sargun A, Bogetti X, Wang J, Achim C, Saxena S. Development of Cu2+-based distance methods and force field parameters for the determination of PNA conformations and dynamics by EPR and MD simulations. J Phys Chem B. 2020;124(35):7544–7556.
66. Bogetti X, Hasanbasri Z, Hunter H, Saxena S. An optimal acquisition scheme for Q-band EPR distance measurements using Cu2+−based protein labels. Phys Chem Chem Phys. 2022. https://doi.org/10.1039/D2CP01032A.
67. Smirnov AI, Belford R, Clarkson R. Comparative spin label spectra at X-band and W-band. Biological Magnetic Resonance. New York: Springer, 2002; p. 83–107.
68. Zhang Z, Fleissner MR, Tipikin DS, et al. Multifrequency electron spin resonance study of the dynamics of spin labeled T4 lysozyme. J Phys Chem B. 2010;114(16):5503–5521.
69. Budil DE, Lee S, Saxena S, Freed JH. Nonlinear-least-squares analysis of slow-motion EPR spectra in one and two dimensions using a modified Levenberg–Marquardt algorithm. J Magn Reson A. 1996;120(2):155–189.
70. Meirovitch E, Nayeem A, Freed JH. Analysis of protein-lipid interactions based on model simulations of electron spin resonance spectra. J Phys Chem. 1984;88(16):3454–3465.
71. Abragam A. The principles of nuclear magnetism. New York: Oxford university press, 1961.
72. Tkachenko NV. Chapter 14 - Polarization measurements. In: Tkachenko NV, editor. Optical Spectroscopy. Amsterdam: Elsevier Science, 2006; p. 249–261.
73. Idiyatullin D, Daragan VA, Mayo KH. Protein dynamics using frequency-dependent order parameters from analysis of NMR relaxation data. J Magn Reson. 2003;161(1):118–125.
74. Bu T, Wang H-CE, Li H. Single molecule force spectroscopy reveals critical roles of hydrophobic Core packing in determining the mechanical stability of protein GB1. Langmuir. 2012;28(33):12319–12325.
75. Zhang Z, Xi X, Scholes CP, Karim CB. Rotational dynamics of HIV-1 nucleocapsid protein NCp7 as probed by a spin label attached by peptide synthesis. Biopolymers. 2008;89(12):1125–1135.
76. Bonucci A, Murrali MG, Banci L, Pierattelli R. A combined NMR and EPR investigation on the effect of the disordered RGG regions in the structure and the activity of the RRM domain of FUS. Sci Rep. 2020;10(1):20956.
77. Izmailov SA, Rabdano SO, Hasanbasri Z, Podkorytov IS, Saxena S, Skrynnikov NR. Structural and dynamic origins of ESR lineshapes in spin-labeled GB1 domain: The insights from spin dynamics simulations based on long MD trajectories. Sci Rep. 2020;10(1):957.
78. Xue Y, Ward JM, Yuwen T, Podkorytov IS, Skrynnikov NR. Microsecond time-scale conformational exchange in proteins: Using long molecular dynamics trajectory to simulate NMR relaxation dispersion data. J Am Chem Soc. 2012;134(5):2555–2562.
79. Singewald K, Wilkinson JA, Saxena S. Copper based site-directed spin labeling of proteins for use in pulsed and continuous wave EPR spectroscopy. Bio-protocol. 2021;11(24):e4258.
80. Mims W. Envelope modulation in spin-echo experiments. Physical Review B. 1972;5(7):2409–2419.
81. Fauth J-M, Schweiger A, Braunschweiler L, Forrer J, Ernst R. Elimination of unwanted echoes and reduction of dead time in three-pulse electron spin-echo spectroscopy. J Magn Reson (1969). 1986;66(1):74–85.
82. Luzik DA, Rogacheva ON, Izmailov SA, Indeykina MI, Kononikhin AS, Skrynnikov NR. Molecular dynamics model of peptide-protein conjugation: Case study of covalent complex between Sos1 peptide and N-terminal SH3 domain from Grb2. Sci Rep. 2019;9(1):20219.

SUPPORTING INFORMATION

Additional supporting information can be found online in the Supporting Information section at the end of this article.

How to cite this article: Singewald K, Wilkinson JA, Hasanbasri Z, Saxena S. Beyond structure: Deciphering site-specific dynamics in proteins from double histidine-based EPR measurements. Protein Science. 2022;31(7):e4359. https://doi.org/10.1002/pro.4359